

## Orientational ordering within semiconducting polymer fibrils

Subhrangsu Mukherjee\*, Eliot Gann, Masrur Morshed Nahid, Terry McAfee, Andrew A. Herzing, Dean M. DeLongchamp\*, Harald Ade\*

S. Mukherjee

Department of Physics, Organic and Carbon Electronics Laboratories, North Carolina State University, Raleigh, NC 27695, USA

Material Measurement Laboratory, National Institute of Standards and Technology, Gaithersburg, MD 20899, USA

E-mail: subhrangsu.mukherjee@nist.gov

E. Gann, A. A. Herzing, D. M. DeLongchamp

Material Measurement Laboratory, National Institute of Standards and Technology, Gaithersburg, MD 20899, USA

E-mail: dean.delongchamp@nist.gov

M. M. Nahid, T. McAfee<sup>[+]</sup>, H. Ade

Department of Physics, Organic and Carbon Electronics Laboratories, North Carolina State University, Raleigh, NC 27695, USA

E-mail: hwade@ncsu.edu

[+] Present address: Advanced Light Source, Lawrence Berkeley National Laboratory, Berkeley, CA 94720

This is the author manuscript accepted for publication and has undergone full peer review but has not been through the copyediting, typesetting, pagination and proofreading process, which may lead to differences between this version and the [Version of Record](#). Please cite this article as doi: [10.1002/adfm.202102522](https://doi.org/10.1002/adfm.202102522).

Keywords: Polarized resonant soft X-ray scattering; scattering anisotropy; fibrils; orientational ordering; crystal-amorphous interphase

Due to a general paucity of suitable characterization methods, the internal orientational ordering of polymer fibrils has rarely been measured despite its importance particularly for semi-conducting polymers. An emerging tool with sensitivity to bond orientation is polarized resonant soft X-ray scattering (P-RSoXS). Here, P-RSoXS reveals molecular arrangement within fibrils (if type I or type II fibrils), the extent of orientation in the fibril crystal, and an explicit crystal-amorphous interphase. Neat films as well as binary blends with a fullerene derivative were characterized for the polymers P3HT, PffBT4T-2OD and PDPP3T, which are prototypical materials widely used in organic electronics applications. Anisotropic P-RSoXS patterns reveal two different fibril types. Analysis of the  $q$ -dependence of the anisotropy from simulated and experimental scattering patterns reveal that neat polymer fibrillar systems likely comprise more than two phases, with the third phase in addition to crystal and amorphous likely being an interphase with distinct density and orientation. Intriguingly, the fibril type correlates to the H- or J-aggregation signature in ultraviolet-visible (UV-Vis) spectroscopy, revealing insight into the fibril formation. Together, the results will open the door to develop more sophisticated structure-function relationships between chemical design, fibril type, formation pathways and kinetics, interfacial ordering, and eventually device functions.

## 1. Introduction

Conjugated organic polymers are increasingly being developed as functional materials for various electrical and optical devices including organic thin film transistors (OTFTs), organic light emitting diodes (OLEDs) and organic photovoltaics (OPVs). Over the past few decades, a key focus has been on tailoring certain properties of organic semiconductors such as mechanical flexibility and thermal or electrical conductivity to fit different applications. Organic conjugated semiconducting polymers have been demonstrated in a wide range of applications such as OPVs,<sup>[1]</sup> electronic paper,<sup>[2]</sup> organic radio frequency identification (RFIDs),<sup>[3]</sup> sensors,<sup>[4]</sup> and large area flexible displays.<sup>[5]</sup> Charge transport in organic electronics occurs both along conjugated chains and in the direction of  $\pi$ -stacking,<sup>[6]</sup> and it is sensitive to short- and intermediate-range order. The structure and orientation of molecules within crystalline and amorphous phases – and between them – is a particularly critical determinant of device performance in organic electronic devices. Device performance optimization

This article is protected by copyright. All rights reserved.

necessitates improved understanding of backbone packing, interfacial ordering, and molecular orientation.

The structure of semicrystalline conjugated polymers is often characterized via microscopy and beam-based scattering methods. Using these methods, it has been widely observed that in high performance OTFT as well as OPV bulk heterojunction (BHJ) systems, the morphology is frequently fibrillar.<sup>[7]</sup> Although real-space confirmation of fibril shape, size, and connectivity is possible through use of specialized ultra-high-resolution electron microscopies,<sup>[8]</sup> these techniques are not sensitive to molecular orientation within the fibrils. Conventional small-angle scattering probes of polymer structure (e.g., hard X-rays, neutrons) are also not sensitive to molecular orientation. Polarized Resonant Soft X-ray Scattering (P-RSoXS), which relies on tensor optical constants near an absorption edge, features high contrast between organic materials with different chemistry, and its access to orientation-based contrast modes promises to overcome challenges in characterizing inter- and intrafibrillar structure in conjugated polymers. The physical principles of composition contrast with resonant soft X-ray scattering (RSoXS) technique have been well demonstrated in glassy block copolymer systems,<sup>[9]</sup> but the P-RSoXS technique (**Figure 1a**) has the promise to go further in the extraction of orientation information from analysis of anisotropy in the scattering intensity correlated to X-ray polarization, which reflects spatial correlations of molecular orientation.<sup>[10]</sup> In P-RSoXS the resonant absorption of soft X-rays results in changes in the complex index of refraction near the resonant energies. The scattering patterns are therefore dependent on energy as well as polarization. For an isotropic sample, such as fibrils randomly oriented in the scattering plane, the scattering pattern is isotropic at non-resonant energies, such as 270 eV. At an energy near the C 1s $\rightarrow\pi^*$  resonance, such as 285.2 eV, the pattern is anisotropic and induced by the polarization of the incident X-rays, with more intense scattering parallel or perpendicular to the electric field vector. If the electric field is rotated, this kind of scattering anisotropy will rotate by the same angle. Such scattering anisotropy has been previously observed in a number of polymer:fullerene systems,<sup>[10b, 11]</sup> and could even be utilized to study phenomenologically the relative degree of molecular orientation relative to the donor-acceptor hetero-interface.<sup>[11a]</sup>

This article is protected by copyright. All rights reserved.

We emphasize that such electric-field imposed scattering pattern anisotropy occurs even if the scattering objects (fibrils) themselves are randomly oriented within the scattering plane about substrate normal. If, instead, the fibrils were also comprehensively aligned in a certain direction, due perhaps to a directional coating process or grooved substrate,<sup>[12]</sup> in what we might call a “structurally biaxial” film, then one would observe scattering pattern anisotropy at non-resonant energies such as 270 eV that would rotate with the *sample* rather than with the electric field vector. At resonant energies, the oriented transition dipoles within a structurally biaxial film would also interact with scattering processes, and might diminish or enhance the scattering anisotropy along the biaxial axes (or even in other directions) depending on the alignment of molecules within the structurally biaxial material and the alignment of the structurally biaxial axes with the electric field vector, in a manner that would rotate with the electric field vector.

Previous accounts of P-RSoXS-derived molecular orientations were typically qualitative and attempted to explain only the “sign” of the single dominant orientation contrast, which was often taken as the preferred orientational arrangement at domain boundaries. In conjugated polymers, the conjugated plane orientation is most often the target, and its orientation was typically described in the familiar terms of “edge-on” or face-on” (in this case with regard to domain boundaries, rather than the substrate as the terms are more often used). This simple treatment,<sup>[11d, 13]</sup> necessary in the early days of developing P-RSoXS analysis frameworks, ignores the common understanding<sup>[14]</sup> that semicrystalline polymers typically exhibit a complicated crystal-amorphous interphase at the edges of crystals, which may have unique orientational properties of its own. A proper analysis thus requires the capability to consider the fibril as a central crystal (core) and a surrounding unique interphase (shell) and separate their impacts on the P-RSoXS result. Such an analysis may be accomplished using the forward simulation of P-RSoXS patterns from real-space models.

This article is protected by copyright. All rights reserved.

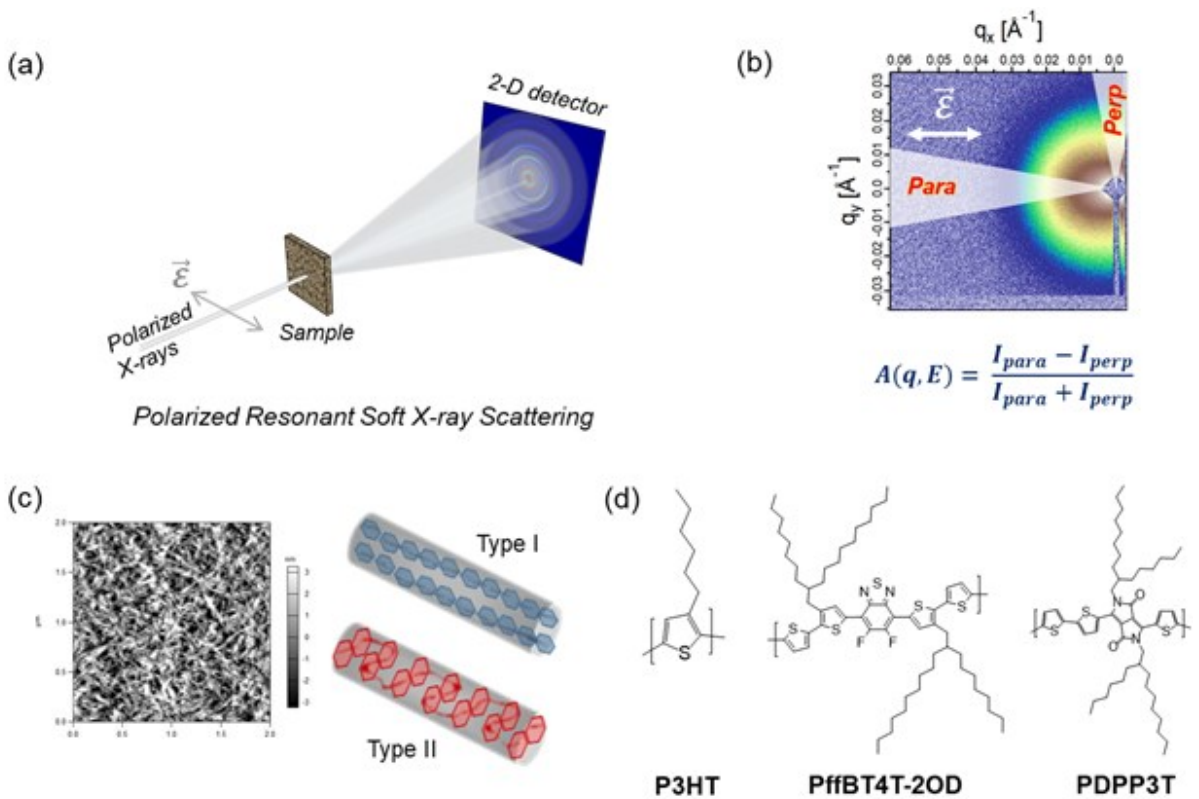


**Figure 1.** (a) Schematic of P-RSoXS experiment; (b) scattering anisotropy parameter at X-ray energy ( $E$ ) in terms of scattered intensity at  $E$  in directions parallel (Para) and perpendicular (Perp) with respect to the electric field ( $\vec{E}$ ) of the incident X-rays. (c) Representative atomic force microscopy (AFM) image of polymer fibrils and schematic differentiation of type I and type II fibrils where the hexagons represent the backbone moieties. (d) Chemical structures of polymers used in this study – P3HT, PffBT4T-2OD, PDPP3T having different repeat lengths - 0.39 nm (regioregular with two thiophene units),<sup>[15]</sup> 1.06 nm, and 0.72 nm respectively.

Here, we advance the analysis framework for P-RSoXS of semiconducting polymers with an approach to treat fibrils as two-part systems with a central crystal and a distinct crystal-amorphous interphase. We focus our study on earlier observations that anisotropy, defined as  $A(q, E) = \frac{I_{\text{para}} - I_{\text{perp}}}{I_{\text{para}} + I_{\text{perp}}}$ , where  $q$  and  $E$  denote momentum transfer and incident X-ray energy respectively (Figure 1b), might have

different signs arising from a type I<sup>[16]</sup> versus a type II<sup>[17]</sup> fibril (see Figure 1c). For this purpose, we require materials and systems that are generally well-characterized, likely to form type I (polymer chains parallel to fibril long axis) or type II (chains orthogonal to fibril long axis) fibrils, as shown schematically in Figure 1c, with characteristic scattering anisotropy,<sup>[11d]</sup> and exhibit differences in UV-Vis aggregation properties. Based on the above properties, three polymers – poly[3-hexylthiophene] (P3HT), poly[(5,6-difluoro-2,1,3-benzothiadiazol-4,7-diyl)-alt-(3,3'''-di(2-octyldodecyl)-2,2';5',2'';5'',2'''-quaterthiophen-5,5'''-diyl)] (PffBT4T-2OD), and poly[2,2'-[(2,5-bis(2-hexyldecyl)-3,6-dioxo-2,3,5,6-tetrahydropyrrolo[3,4-c]pyrrole-1,4-diyl)dithiophene]-5,5'-diyl-alt-thiophen-2,5-diyl] (PDPP3T) – that are well-known for their use in OPV<sup>[7e, 18]</sup> and/or OTFT<sup>[19]</sup> applications and relatively straightforward to process to form fibrillar structures were chosen for the study. The chemical structures of the polymers are shown in Figure 1d.

Comparing the  $q$ -dependence of the scattering anisotropy observed in experimental data from neat films and blends of the three polymers with fullerene, and forward simulation of P-RSoXS using the core-shell fibril model, we differentiate between the different material and/or density phases present in the samples as well as extent of orientation within the fibrils. Interestingly, even neat polymer systems are found to consist of three phases including two distinct density phases. Furthermore, the energy dependence of the scattering anisotropy for the three polymers enables us to distinguish between packing of polymer chains in type I vs type II fibrils that can be detected even in homo-material thin films. The results can be correlated with the optical aggregation properties and have implications on extraction of densities and volume fractions of different phases in a system that are key towards understanding of fibril formation and polymer crystallization processes in general.

## 2. Results and discussion

The packing of the polymer backbone is different within type I and type II fibrils. In type I fibrils the polymer chain backbone packs parallel to the fibril long axis whereas in type II fibrils the backbone is

orthogonal to the fibril long axis. Microscopy of films of neat P3HT, PffBT4T-2OD, and PDPP3T polymers as well as the blends with fullerene derivatives ([6,6]-Phenyl-C61-butyric acid methyl ester ( $\text{PC}_{61}\text{BM}$ ) or [6,6]-Phenyl-C71-butyric acid methyl ester ( $\text{PC}_{71}\text{BM}$ )) reveal randomly oriented fibrillar structures, as shown in **Figure 2**. All the samples show the presence of a semi-random network of polymer fibrils having average length in the range  $\approx 200$  nm to 400 nm and average fibril widths in the range  $\approx 20$  nm to 40 nm. Although it provides a useful measure of fibril size, shape, and connectivity, this microscopy method does not measure molecular orientation inside the fibrils.

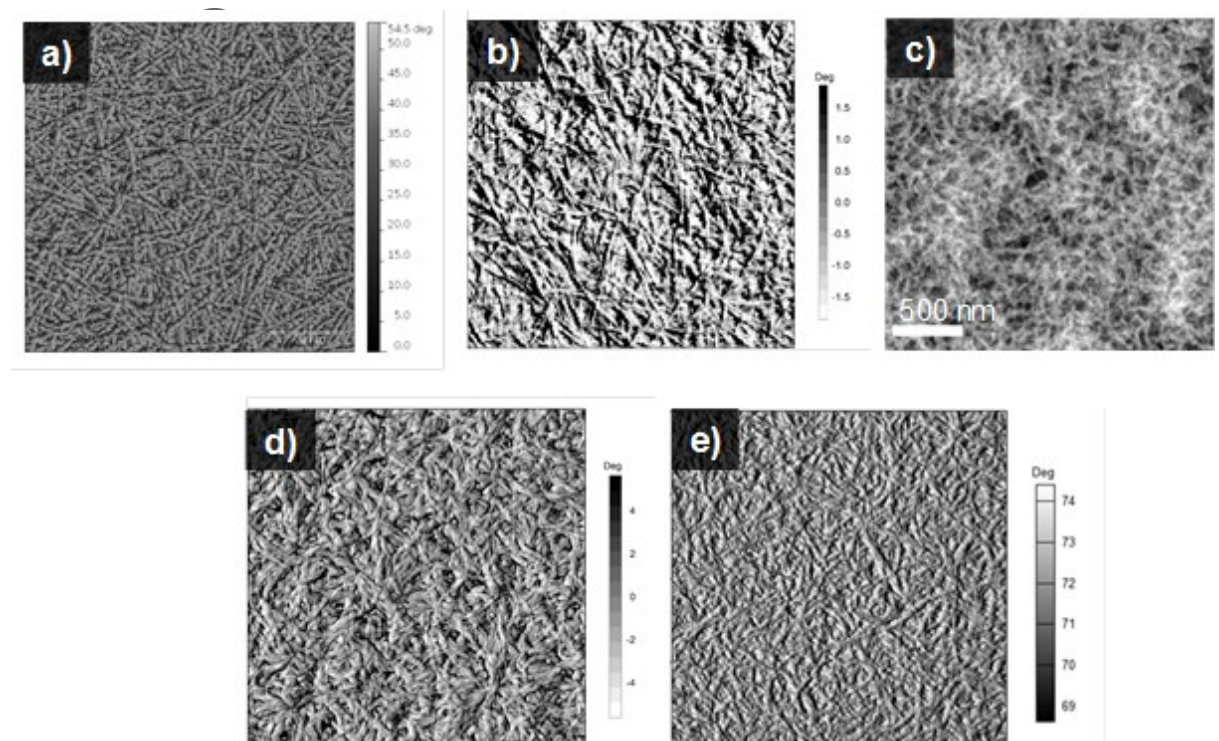


**Figure 2.** AFM phase images ( $2 \mu\text{m} \times 2 \mu\text{m}$ ) of (a) P3HT: $\text{PC}_{61}\text{BM}$  blend film, (b) P3HT neat film. (c) Low-Angle Annular Dark-Field Scanning Transmission Electron Microscopy (LAADF-STEM) image of PffBT4T-2OD: $\text{PC}_{71}\text{BM}$  blend film (scale bar, 500 nm).  $2 \mu\text{m} \times 2 \mu\text{m}$  AFM phase images of (d) PffBT4T-2OD neat film, and (f) PDPP3T neat film.

## 2.1 P-RSoXS of polymer-fullerene blends

We first establish the determination of fibril type by using the prototypical P3HT:PC<sub>61</sub>BM system. The availability of angle dependent near edge X-ray absorption fine structure (NEXAFS) reference data<sup>[20]</sup> for P3HT enables the necessary simulations. **Figure 3** shows the experimental energy dependent anisotropy of P3HT:PC<sub>61</sub>BM blends as 2D patterns, and sector averaged (Para and Perp) 1-D profiles for select energies and an anisotropy vs.  $q$ ,  $E$  map, with corresponding simulations of P3HT:PC<sub>61</sub>BM blends with type II fibrils with no complex structure. The anisotropy maps shown in Figures 3e and 3f are obtained from anisotropy values calculated at each measured/simulated  $q$  and X-ray energy using the energy dependent sector averaged 1-D profiles. We observe overall excellent agreement in the energy dependence of the anisotropy, which directly implies that P3HT forms type II fibrils in P3HT:PC<sub>61</sub>BM blends. Nevertheless, there are some subtle differences. In particular, the data has some inversion of the sign as a function of  $q$  at certain energies, which needs to be further understood by using more sophisticated modeling.

Author Manuscript

This article is protected by copyright. All rights reserved.

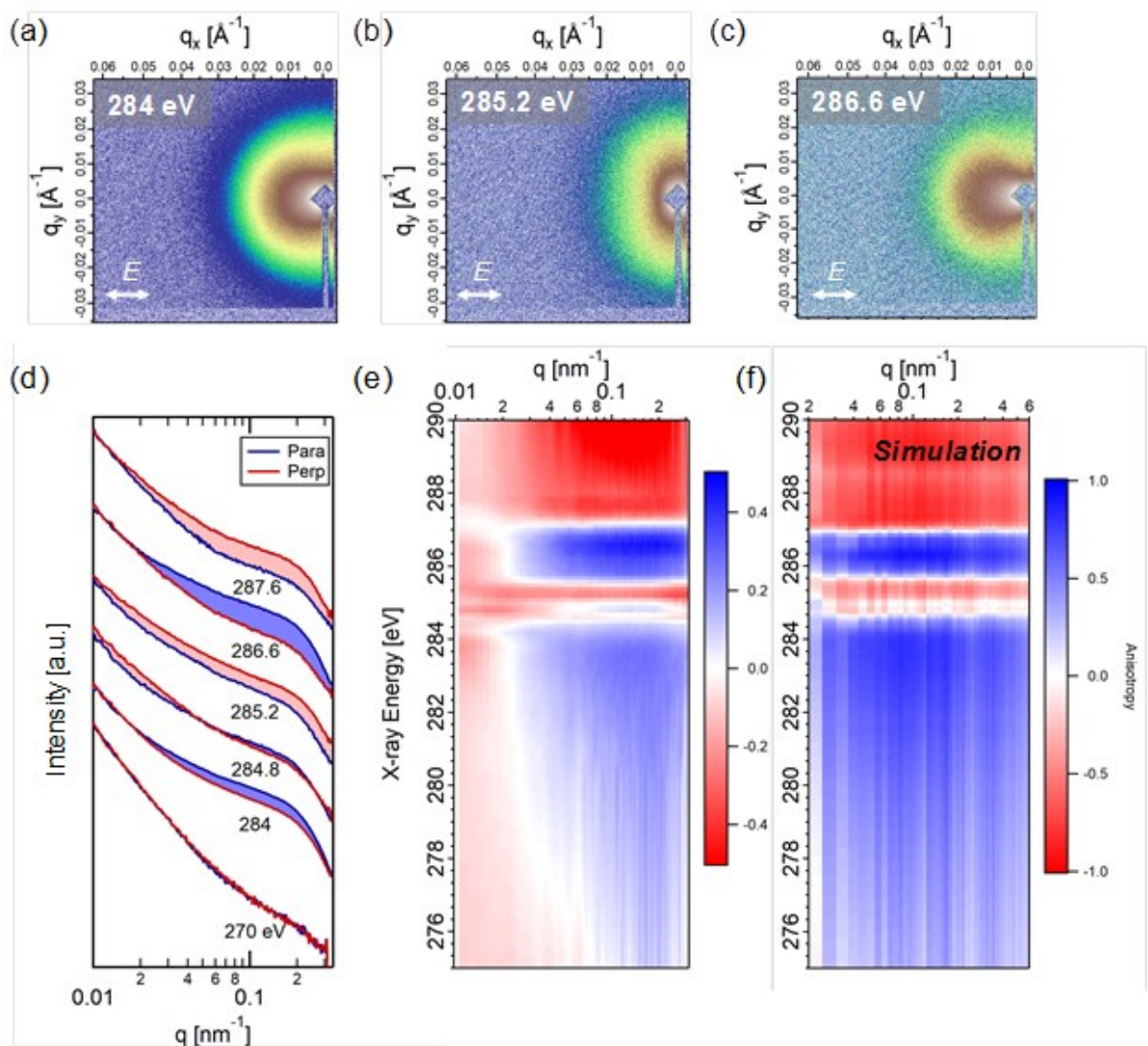


**Figure 3.** (a) – (c) 2-D experimental scattering patterns from a P3HT:PC<sub>61</sub>BM blend at selected energies acquired with horizontally polarized X-rays. (d) 1-D profiles at select energies from 20° sectors parallel (Para) and perpendicular (Perp) to the polarization direction calculated from the 2-D scattering patterns. The intensity difference between the two sectors is highlighted with blue (red) when the scattered intensity is higher in the direction parallel (perpendicular) to the electric field of the incident radiation. The profiles at the different energies are offset vertically for clarity. 2-D anisotropy map as function of  $q$  and incident X-ray energy from (e) experimental and (f) simulated scattering patterns on P3HT:PC<sub>61</sub>BM blends having P3HT fibrils.

In order to investigate the  $q$ -dependence observed above and differences between various materials systems, the 2-D P-RSoXS data from films PffBT4T-2OD and PDPP3T blended with PC<sub>71</sub>BM alongside the 1-D sector-averaged profiles parallel and perpendicular to the electric field of the horizontally polarized incident X-rays at some key energies across the C K-edge are shown in **Figure 4**. They are complemented with data from a P3HT:PC<sub>61</sub>BM blend sample annealed at 80 °C for 20 min (P3HT Blend 80C) that is slightly different compared to the experimental data in Figure 3. The latter was from a sample that was annealed at 150 °C for 20 min (P3HT Blend 150C). The two P3HT blend datasets illustrate variations between samples having the same composition but different processing. The 2-D patterns shown were obtained near the C 1s- $\pi^*$  absorption peak energies of the backbone  $\pi$ -manifold in the range 285 eV to 286 eV.<sup>[21]</sup> The scattering patterns for all the samples is observed to be anisotropic at resonant and near resonant energies. The maximum anisotropy occurs near the peak of  $\pi$ -manifold absorption (285 eV to 286 eV) where the orientation contrast between edge-on and face-on backbone orientations of the polymer relative to the fullerene is maximum as has been observed earlier in a number of polymer:fullerene blend systems.<sup>[10b, 11a, 11c]</sup> In case of the P3HT Blend 80C blend film, the enhanced scattering is generally parallel to the direction of the polarization (positive anisotropy), whereas for the PffBT4T-2OD or PDPP3T blend samples enhanced intensity is perpendicular to the polarization (negative anisotropy). Besides the differences in the sign of the anisotropy, we also note considerable differences in the  $q$ -dependence of the anisotropy between the samples. At 270 eV, the scattering features observed are dominated by mass-thickness (density and thickness variations). The scattering peaks in all the datasets arise from fibril long axis at larger length scales (lower  $q$  values) and fibril diameter or form factor at smaller length scales (higher  $q$  values). Note that the anisotropy changes sign in the case of PffBT4T-2OD:PC<sub>71</sub>BM, and PDPP3T:PC<sub>71</sub>BM when the energy switches from transitions dominated by the aromatic backbone (285 eV to 286 eV) to the sidechains ( $\approx$  288 eV). A key difference is that the anisotropy in the case of P3HT decreases to zero at low and high- $q$  extremities, whereas in PffBT4T-2OD the anisotropy increases first and then stays relatively constant without decreasing to zero at high  $q$ , and in PDPP3T the anisotropy slightly increases at higher  $q$ . This effect is strongest in the C 1s- $\pi^*$  energy range (285 eV to 286 eV) that corresponds to the absorption of the aromatic backbone. The sign of the

anisotropy is also different, with P3HT having positive, and PffBT4T-2OD and PDPP3T negative anisotropy. The length scale corresponding to  $q = 0.4 \text{ nm}^{-1}$  where the differences are most pronounced is 15 nm. This is smaller than the average fibril width and/or spacing. We also note that grazing incidence wide angle X-ray scattering (GIWAXS) shows similar preferred edge-on orientation of the polymer chains with respect to the substrate plane for the P3HT and PffBT4T-2OD blend samples (Figure S1). The three materials have clearly rather different P-RSoXS characteristics that must relate to the internal organization of the fibrils.

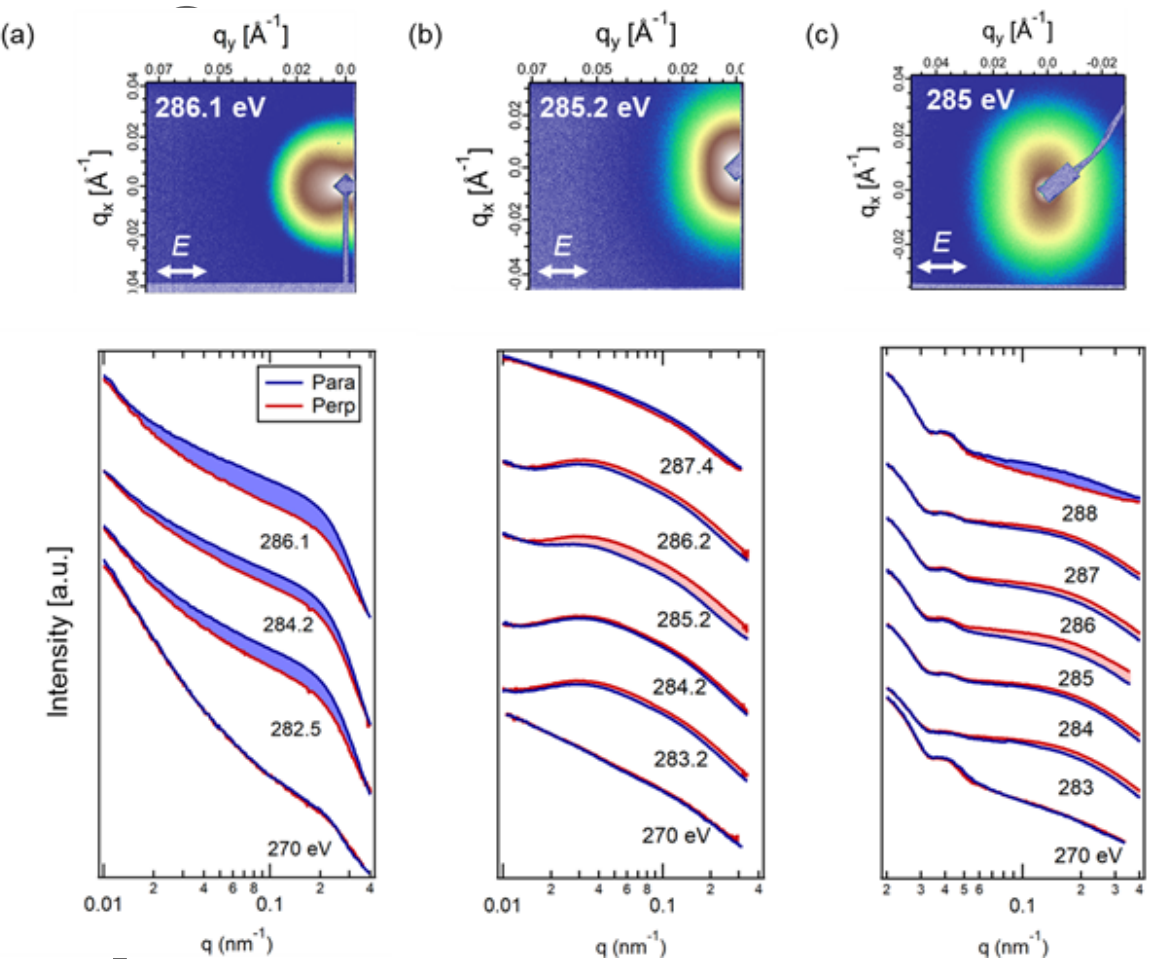


**Figure 4.** P-RSoXS 2-D images (top panel) and 1-d profiles at select energies (bottom panel) obtained from 20° sectors parallel (Para) and perpendicular (Perp) to the direction of polarization of the

electric field (horizontally polarized, as shown) of the incident X-rays for (a) P3HT:PC<sub>61</sub>BM (P3HT Blend 80C), (b) PffBT4T-2OD:PC<sub>71</sub>BM, and (c) PDPP3T:PC<sub>71</sub>BM blends, respectively. The profiles at the different energies are offset vertically for clarity.

## 2.2 P-RSoXS of neat polymer films

Neat films of the three polymers having fibrillar structures were then studied to observe and determine differences between the three systems and differences due to different film formation kinetics in the absence of the fullerene. The morphological appearance and molecular packing and texture of the fibrils was confirmed to be similar to the blends from AFM (Figure 2) and GIWAXS (Figure S2) measurements, respectively. The scattering pattern for the samples are anisotropic at resonant energies and isotropic at non-resonant energies. In order to obtain a more exhaustive picture, the experiments were performed over a wide energy range and with a large number of measurements. The energy dependence of the integrated scattering intensity for the P3HT homomaterial sample is similar to the orientation contrast function calculated from angle dependent P3HT NEXAFS spectra as shown in Figure S3. At the same time, the scattering intensity for PffBT4T-2OD and PDPP3T did not track mass-thickness contrast. This confirms that the scattering at resonant energies is dominated by orientation contrast between differently oriented regions in the films and not due to mass-thickness/density differences.

The 2-D P-RSoXS pattern from the neat films of the three polymers acquired with horizontally polarized X-rays at 285.2 eV are shown in **Figure 5** (top panel). The resulting 2D anisotropy vs.  $q$ , E maps are shown in Figure 5 (bottom panel). Two main observations stand out: (1) the overall sign of the anisotropy for P3HT is different from that of PffBT4T-2OD and PDPP3T; (2) the  $q$ -dependence of each material has a unique signature.

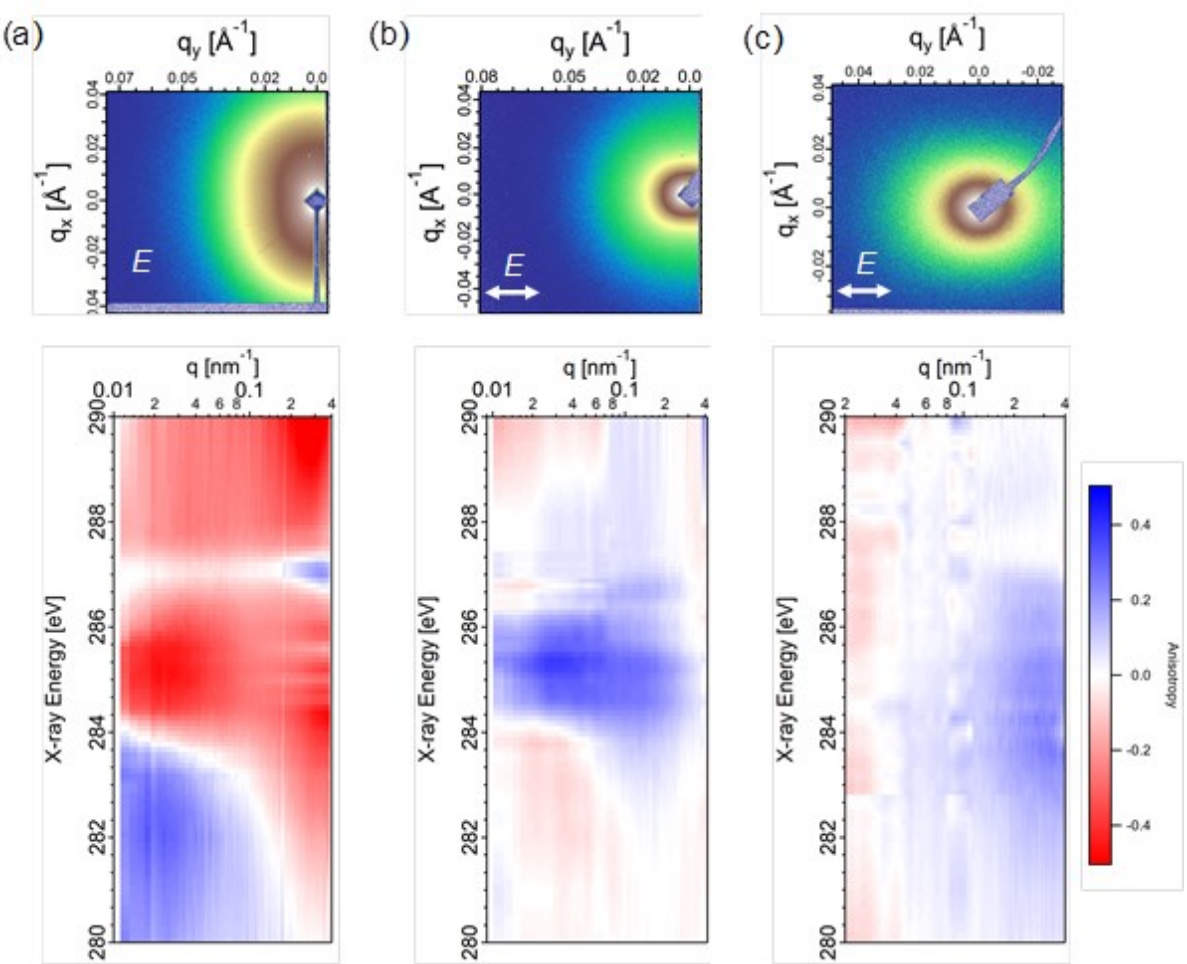


**Figure 5.** (Top) P-RSoXS 2-D data acquired at an energy (285.2 eV) with high orientation contrast from neat polymer films – (a) P3HT, (b) PffBT4T-2OD, and (c) PDPP3T. The electric field polarization direction is indicated in the figures. (Bottom) P-RSoXS anisotropy vs.  $q$ ,  $E$  maps obtained from 20° sectors parallel and perpendicular to the direction of polarization of the electric field of the incident X-rays for the three neat samples (P3HT – left, PffBT4T-2OD – middle, and PDPP3T – right).

Similar to the blends, the anisotropy for the homo-materials show unique energy dependence between the materials. Overall, the anisotropy extrema occur in the energy range of C 1s- $\pi^*$  absorption and there seems to be a tendency to change sign at energies that correspond the limits of the C 1s- $\pi^*$  resonance transition corresponding the backbone. The signal for PDPP3T is relatively

weak and the pattern is not as clear. As before for the blends, the scattering anisotropy rotates with the electric field (Figure S4) which proves the absence of any global alignment in the films. We also note significant differences between the different polymers in the  $q$ -dependence of the scattering anisotropy in the 2D maps. 1-D sector averaged scattering profiles, and anisotropy vs  $q$  plots at resonant and non-resonant energies are shown in Figures S5 and S6. Focusing on the anisotropy at the C 1s  $\pi^*$  resonance, the anisotropy for the PffBT4T-2OD sample is maximum near the scattering peak and decreases at higher  $q$  ( $> 0.2 \text{ nm}^{-1}$ ) values. In contrast, the major contribution to the anisotropy for the PDPP3T and P3HT sample is seen to originate from high- and low- $q$  extremes on the  $q$  scale, respectively.

### 2.3 P-RSoXS simulations – blend and neat systems

Semicrystalline polymer fibrils are expected to organize with a central crystal and a crystal-amorphous interphase. Borrowing language from typical treatments of complex small-angle scattering form factors,<sup>[22]</sup> we will hereafter refer to the central crystal as a “core” and the interphase as a “shell”. In order to determine the origin of the  $q$ -dependence in the experimental data and its relation to the number of phases present in the samples, P-RSoXS simulations were performed with fibrils with this core-shell structure. The fibril width for all simulations was normally distributed with mean 30 nm and standard deviation of 10 nm. The effect of the presence of multiple phases on the  $q$ -dependence of scattering anisotropy was investigated by simulating two and three phase systems. Two-phase blend or neat systems for the simulations comprised core-only polymer fibrils (width of oriented core = fibril diameter, no shell) in an isotropic, amorphous PC<sub>71</sub>BM or polymer matrix, respectively. Three-phase systems were simulated with an oriented core (phase 1), an isotropic shell (phase 2), and an isotropic matrix (phase 3). For the 3-phase blend simulations, the isotropic PC<sub>71</sub>BM matrix was used, whereas for the 3-phase neat simulations the isotropic polymer with a mass density somewhat lower than the crystal was used.

To describe conjugated polymer orientation, we used the uniaxial dielectric function that is developed in **Figure 6**. For the extraordinary axis we isolate  $1s \rightarrow \pi^*$  transition dipole; this important resonance describes the orientation of the pi-plane normal and it is typically found to exhibit polar orientation in NEXAFS spectroscopy of conjugated polymers. Importantly, the extraordinary axis here is *orthogonal* to the backbone long axis. The backbone long axis and the conjugated plane short axis are mixed in the ordinary axes of the dielectric function. In later illustrations, we will depict the orientation of the extraordinary axis but these orientations should be understood as orthogonal to the backbone orientation.

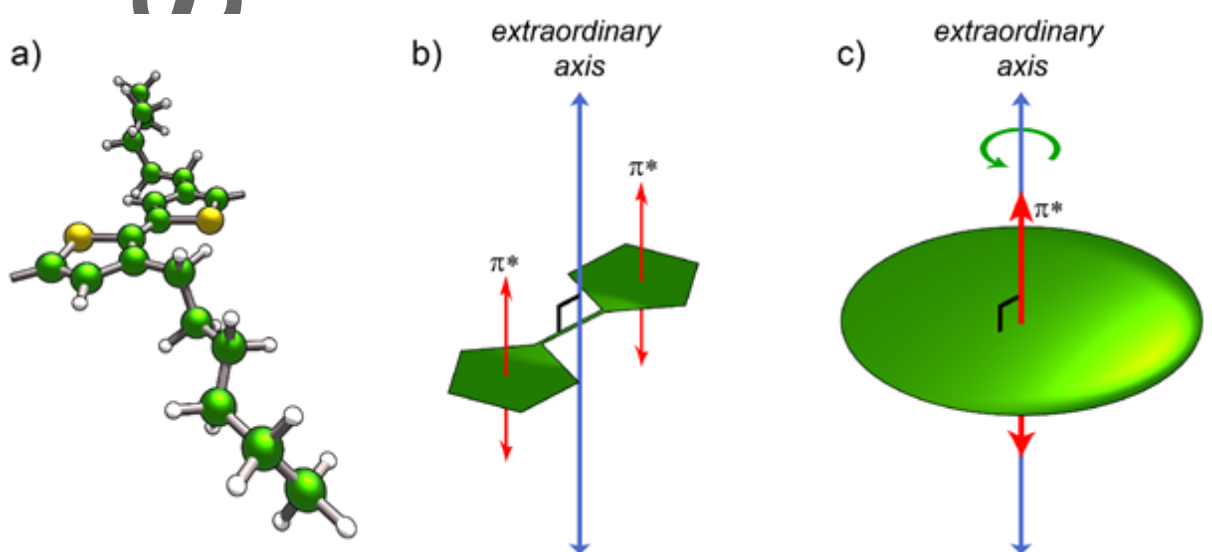


**Figure 6.** Uniaxial dielectric function definition for our conjugated polymers. (a) Molecular illustration of the P3HT molecule. (b) Depiction of coplanar thiophene rings in such a molecule with a common direction for the  $1s \rightarrow \pi^*$  transition dipole parallel to the extraordinary axis. (c) Uniaxial dielectric function obtained by assuming free rotation of the picture in (b) about the extraordinary axis.

Applying this dielectric function to the proposed simulation morphologies, we find that the anisotropy ratio  $A(q)$  for 2-phase blend or neat system is almost constant across the simulated  $q$ -

range, or in other words, shows no  $q$ -dependence. On the other hand, the anisotropy from a 3-phase morphology exhibits significant  $q$ -dependence including sign flip(s) with  $q$  at certain energies.

The 2-phase and 3-phase blends morphology illustrations and the simulated scattering profiles at selected resonant and non-resonant energies are shown in the top and the bottom panel of **Figure 7** respectively. The mean spacing between fibrils was  $\approx 250$  nm and size of each voxel was 5 nm. The optical constants for the dielectric function were taken from a database<sup>[21]</sup> and therefore may not reflect the exact density, composition and orientation distribution in the actual samples. However, the range of resonant and non-resonant energies should be generally similar.

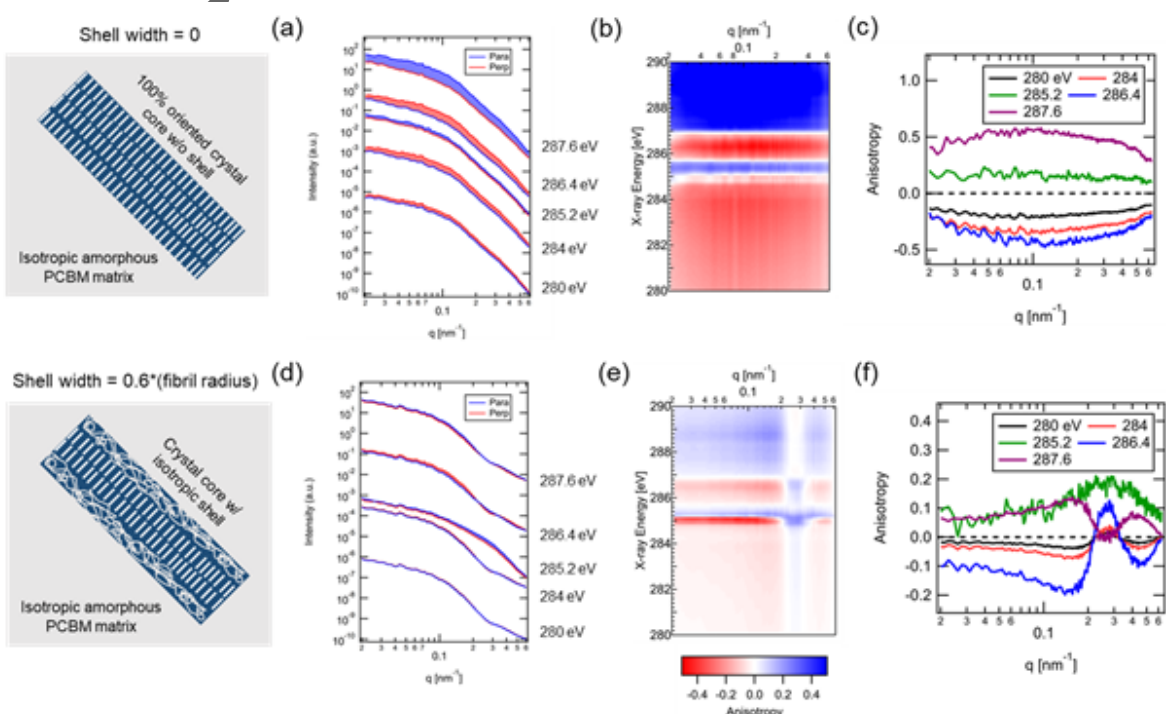


**Figure 7.** P-RSoXS simulations of type I fibrils with 100% orientation (top), type I fibrils with an oriented core and isotropic shell where the width of the oriented core = 40 % of fibril radius (bottom). (a), (d) 1-D scattering profiles at select energies in directions parallel (Para) and

perpendicular (Perp) to the electric field. (b), (e) 2-D anisotropy vs.  $q$ , E maps. (c), (f) 1-D Anisotropy vs  $q$  profiles for both cases. Isotropic PC<sub>71</sub>BM was chosen as the matrix. Morphology schematics are shown in the left panel. The fibrils comprise in-plane polymer chains with edge-on lamella. The short white straight lines inside the fibrils represent the dielectric function extraordinary axis projected onto the cross-sectional plane and random white lines represent the isotropic polymer in the shell. The 1-D scattering profiles at the different energies in (a) and (d) are offset vertically for clarity.

The simulations reveal a significant difference in the nature of the  $q$ -dependence between the two cases – fibrils with and without an isotropic shell around the oriented core. The effects are strongest in the energy range 284 eV to 288 eV in the simulations. The above results therefore indicate that the main differences in  $q$ -dependence of the experimental data originate from microstructure within the fibrils where we either have oriented polymer chains throughout the bulk of the fibrils or an outer shell/crystal-amorphous interphase of isotropic chains around an oriented fibril core. We note that this is a form factor effect that can be understood relatively easily and intuitively. The expression for the form factor of a core-shell cylinder<sup>[22]</sup> is

$$P(q) = \frac{\text{scale}}{V_{\text{shell}}} \int_0^{\pi/2} f^2(q) \sin \alpha \, d\alpha + bkg$$

where,

$$f(q) = \\ 2(\rho_{\text{core}} - \rho_{\text{shell}})V_{\text{core}} \frac{\sin(qL\cos(\frac{\alpha}{2}))}{qL\cos(\frac{\alpha}{2})} \frac{J_1(qrsin\alpha)}{qrsin\alpha} + 2(\rho_{\text{shell}} - \\ \rho_{\text{solvent}})V_{\text{shell}} \frac{\sin(q(L+2t)\cos(\frac{\alpha}{2}))}{q(L+2t)\cos(\frac{\alpha}{2})} \frac{J_1(q(r+t)\sin\alpha)}{q(r+t)\sin\alpha} \quad (1)$$

# Author Manuscript

This article is protected by copyright. All rights reserved.

and  $r$ ,  $L$ ,  $V$ ,  $t$  are the cylinder radius, length, volume and shell thickness respectively,  $\rho$ 's are polarization dependent scattering length densities,  $\alpha$  is the angle between momentum transfer vector and cylinder long axis, and  $J_1$  is the first order Bessel function of the first kind. The anisotropy at high  $q$  is the superimposition of the form factors of the two orthogonal orientations of a fibril (see Figure S7 and related discussion in SI). Further improved modeling that matches the data even better might require accounting for more complex intra- and inter-molecular order and aggregation<sup>[23]</sup> or a population distribution of different fibrils where fibril type or internal organization might be coupled to fibril size. Of particular note is that, although we have modeled the crystal-amorphous interphase here as isotropic for establishing the basic phenomenology, a similar 3-phase type pattern could be obtained with different degrees of orientation and densities within the interphase. Such complexity is beyond the scope of this study but provides a rich landscape of fitting opportunities for future studies. Differences in the sign of the anisotropy and its possible relation to the  $q$ -dependence will be further explored and discussed below in the context of P-RSoXS results from neat polymer films.

Simulations for neat type II fibrils having an oriented core and an isotropic shell using angle-dependent optical constants for P3HT are shown in **Figure 8**. In one case the shell is contrast matched with the matrix i.e., the optical constants of the shell and matrix are identical and none/negligible energy or  $q$ -dependence of the anisotropy was observed (Figure 8, top panel). A system consisting of oriented polymer core (phase 1), and an amorphous shell that is contrast-matched to the matrix (phase 2) is a two-phase system. In order to simulate a 3-phase neat polymer system the contrast between the matrix and the isotropic shell needs to be non-zero. Differences in mass density affect the optical constants and can result in a non-zero density contrast between two phases that are otherwise identical. It may be noted here that different amorphous phases of P3HT have been observed before.<sup>[24]</sup> It is likely that there are density differences between the isotropic shell in the fibril and the isotropic matrix in the neat polymer samples. In our simulations, when the density of the amorphous matrix was set to a lower value than the isotropic shell a  $q$ -dependence as well as an energy dependence of the anisotropy was observed (Figure 8, bottom panel). We note that the second case represents a 3-phase system - oriented polymer core (phase 1), isotropic

amorphous shell (phase 2), and amorphous matrix with a different mass density (phase 3). Apart from the optical constants of the matrix all other parameters (fibril size, spacing, polydispersity, radius, and volume fraction) were held constant between the simulations.

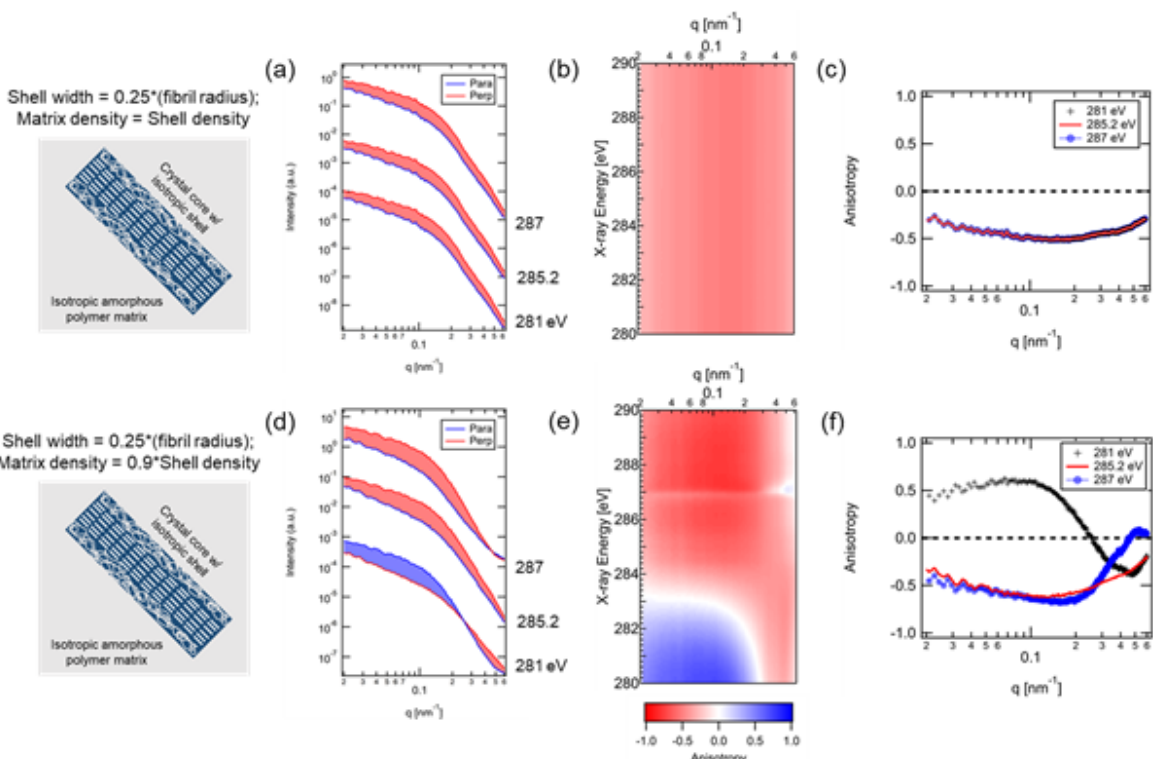


**Figure 8.** Simulation results for P3HT type II fibrils with an oriented core and isotropic shell in P3HT matrix. The matrix density = shell density (top), and matrix density < shell density (bottom). (a), (d) 1-D scattering profiles at select energies in directions parallel (Para) and perpendicular (Perp) to the electric field. (b), (e) 2-D anisotropy vs.  $q$ , E maps. (c), (f) 1-D Anisotropy vs  $q$  profiles. Shell thickness was set at 25 % of fibril radius for both cases. Morphology schematics are shown in the left panel. The fibrils comprise in-plane polymer chains with edge-on lamella. The short white straight lines inside the fibrils represent the dielectric function extraordinary axis projected onto the cross-sectional plane and random white lines represent the isotropic polymer in the shell. The 1-D scattering profiles at the different energies in (a) and (d) are offset vertically for clarity.

The best match between the experiment and simulations for the P3HT neat film was obtained when the mass density of the matrix was set equal to 90 % of the mass density of the fibril (shell or core) and shown in **Figure 9**. Comparison of the  $q$  and energy dependence of the experimental and simulated anisotropy therefore suggests that all the fibrils in our study consist of isotropic chains in their core and lesser degrees of orientation in the shell. The densities of the shell and matrix are also likely different in the neat films. Again, we note that we consider only isotropic shells in as prototypical models, but different degrees of orientation and densities within the interphase could produce similarly switching patterns having unique anisotropy trends in anisotropy with energy and  $q$ .

Thus our models show that the experimental P-RSoXS data of the neat polymers can only be reproduced in simulation if three phases are present: 1) an oriented core, and 2) an isotropic shell having the same density but between which orientation contrast is possible, and 3) an isotropic matrix which has orientation contrast with the core and density contrast with both the core and the shell. These results imply that the polymer fibril:fullerene blend systems are also likely composed of more than three phases. Overall, the PDPP3T fibrils have similar core-shell width ratios in neat and blend, but the orientation is increased (larger anisotropy) in the blend when the fibrils form in the presence of a second material that is phase separating. This is consistent with recent results in PDPP3T blends with polystyrene,<sup>[25]</sup> where improved molecular packing has been observed in blends with high polystyrene content. The PffBT4T-2OD fibrils are oriented in the core, have similar overall strength of the anisotropy, but dissimilar core and shell width ratios in the neat and in the fullerene blend. The strong temperature-dependent aggregation of PffBT4T-2OD seems to make fibril formation relatively insensitive to the presence or absence of a second material, and only the details of the internal structure change but not the strong tendency to form fibrils. The P3HT fibrils are also mostly oriented in the core but the lower anisotropy at higher- $q$  suggest that the fibrils are closer to 100% oriented fibrils with a relatively thinner shell compared to PDPP3T and PffBT4T-2OD fibrils. The

differences observed between neat and blend films indicate that the dynamics of morphology evolution and fibril formation during casting might be significantly different for the three materials.

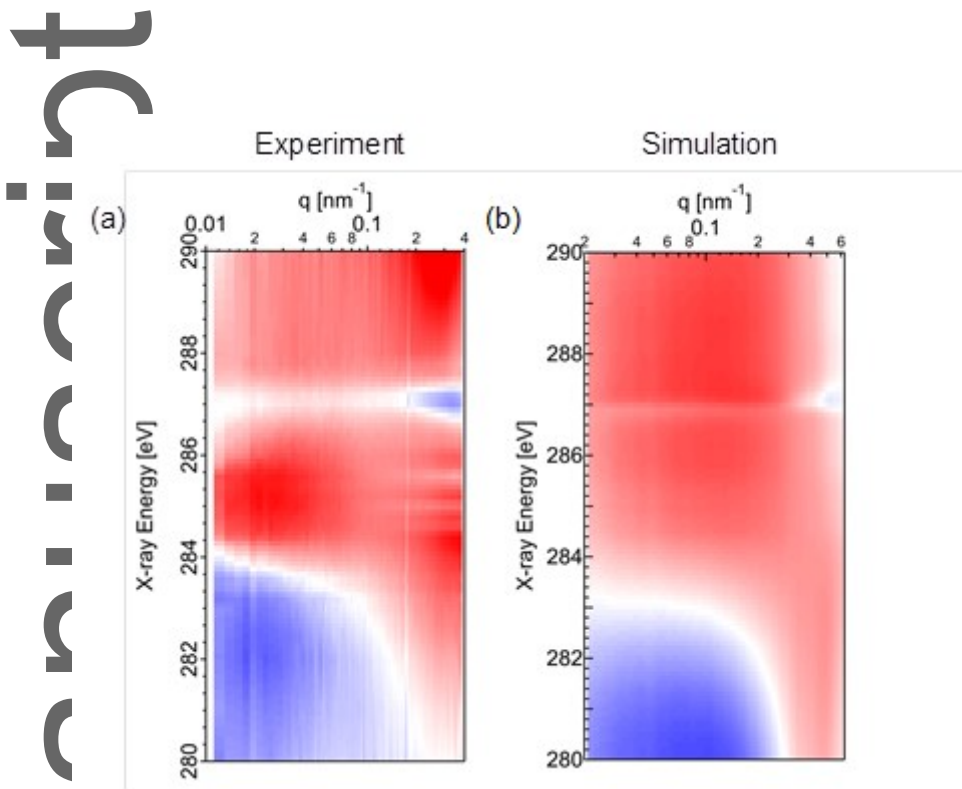


**Figure 9.** Comparison of 2-D anisotropy maps from (a) experiment, and (b) optimal simulations for neat P3HT sample. The optimal simulation results were obtained when the mass density of the matrix was set equal to 90 % of the mass density of the fibril (shell or core) in the simulations.

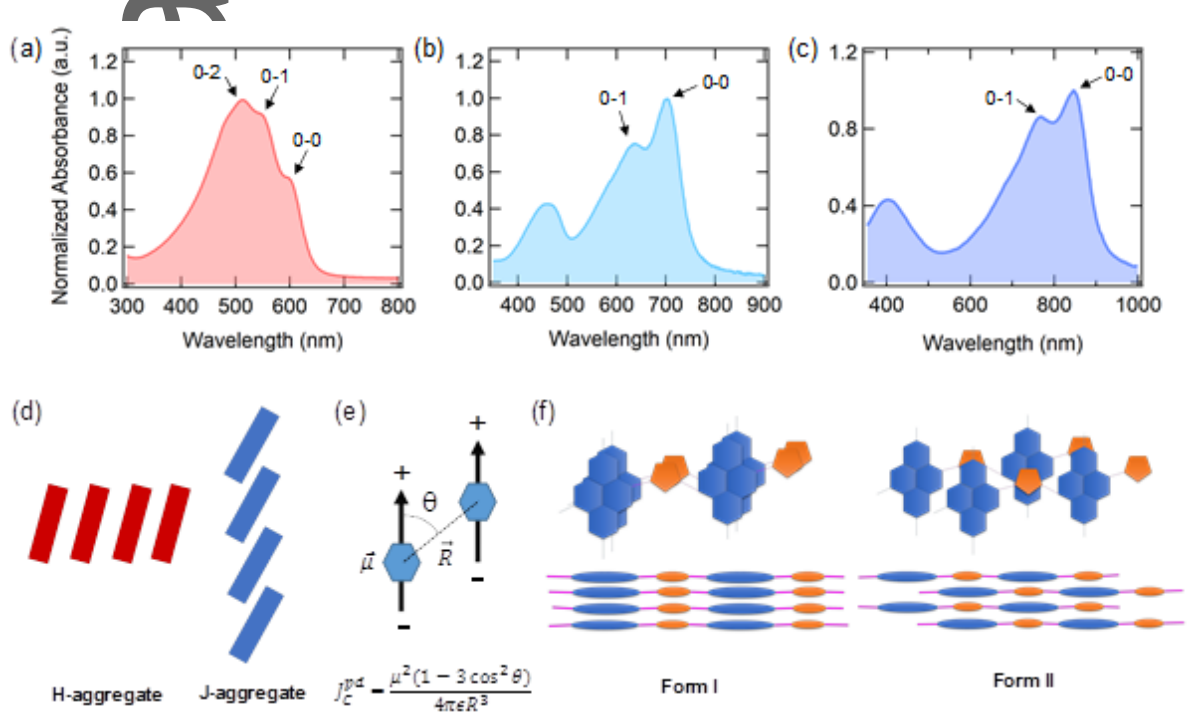
#### 2.4 Fibril formation and optical aggregation signature

Finally, we explore the origins of fibril organization into type I and type II. The primary factor should be the relative growth rates of the in-plane crystal axes, which are controlled by molecular design and intermolecular potentials. Secondary factors might also play a role, including solvent choice, evaporation rate, temperature, stiffness/persistence length, and molecular weight. We cannot explore all the factors, but we believe that some relevant relations or hypotheses can be established for the fibril organization that will guide more detailed studies in the future. We start by noting that

the persistence length of P3HT, PffBT4T-2OD, and PDPP3T can be calculated from dihedral potentials to be 4.1 nm, 2.9 nm, and 24.7 nm,<sup>[26]</sup> respectively. Clearly, PDPP3T is comparatively rather stiff. It is a material unlikely to form backfolded stacked lamella with the fast growth direction perpendicular to the polymer backbone. PDPP3T will therefore tend to form type I fibrils due to its large persistence length. In contrast, P3HT is known to be able to form backfolding lamella (type II),<sup>[23]</sup> which is easily facilitated by its small persistence length. The observation that PffBT4T-2OD forms type I fibrils rather than type II fibrils seems to be at odds with this simplistic description, given its small persistence length. Additional parameters must be considered, such as its alternating co-polymer backbone structure when compared to P3HT. Overall, the repeat length along the backbone increases from 0.39 nm to 1.06 nm, a difference of a factor of 2.7. Furthermore, in a donor-acceptor push-pull copolymer, there are two principal nearest neighbor chain stacking patterns.<sup>[27]</sup> In PffBT4T-2OD, the BT and 4T moieties can be either stacked adjacent to each other or in a staggered fashion. These are at times referred as form I and form II polymorphs.<sup>[27c]</sup> If the material has a clear preference for either of these polymorphs, backfolding is entropically and possibly geometrically constrained due to the large repeat length along the backbone and the effective persistence length during self-assembly might be increased.

In order to measure the molecular packing and relate it to a preferred polymorph, we compare the optical aggregation signature of P3HT, PffBT4T-2OD, and PDPP3T. The relative intensities of the nominal 0-0 and 0-1 peaks in the optical spectra from the P3HT and PffBT4T-2OD neat films reveal H- or J-aggregation, respectively.<sup>[7g, 28]</sup> It is well-known<sup>[28b]</sup> that in H-aggregated P3HT the nearest-neighbor chromophores in the conjugated backbone are oriented in an eclipsed (form I) rather than staggered (form II) side-by-side arrangement. In contrast, in J-aggregates the neighboring chromophores in the polymer backbone are oriented in a more head-to-tail manner. The aggregation is described within the Kasha model by the coupling constant  $J_c$  derived from geometric interaction of two dipoles (see **Figure 10**).<sup>[29]</sup> If one considers a chromophore to be the repeat moieties in the polymer backbone, i.e., the (001) spacing, the spacing of chromophores along the backbone would be 1.06 nm and 0.72 nm for PffBT4T-2OD and PDPP3T, respectively. In contrast, the  $\pi$ - $\pi$  stacking distance is 0.35 nm. Given its  $R^3$  scaling,  $J_c$  is clearly dominated by the interactions

between dipoles on neighboring chains and not between dipoles along the backbone. A simple geometric consideration, assuming an orthorhombic system, would result in,  $\theta = \tan^{-1} \left( \frac{d_{010}}{d_{001}} \right)$ , where  $d_{hkl}$  is the lattice spacing. It follows that J-aggregated materials such as PffBT4T-2OD and PDPP3T have a strongly staggered geometric arrangement of their dipoles with  $\theta < 45^\circ$ , indicating a form II polymorph. The absence of any H-aggregated populations in the UV-Vis of PffBT4T-2OD and PDPP3T indicates that the form II polymorph is strongly preferred.<sup>[30]</sup> This strong preference for one type of aggregation then constraints the backfolding of the PffBT4T-2OD and the fibrils are formed by aggregation of separate chains, a process that leads to the fastest fibrillar growth parallel to the backbone rather than in the  $\pi$ - $\pi$  stacking direction (type II). We note that the tendency to orient within the core versus the shell is correlated to the fibril type and polymorph, indicating very different self-assembly pathways. Deeper understanding of the details for the fibril formation kinetics and pathways requires additional research. Future studies comprising a combination of in-situ UV-Vis and in-situ GIWAXS, coupled to ex-situ P-RSoXS would likely provide deeper insights.



This article is protected by copyright. All rights reserved.

**Figure 10.** UV-Vis absorbance spectra from (a) P3HT, (b) PffBT4T-2OD, (c) PDPP3T neat films. (d) Molecular orientations in H- and J-aggregates. (e) Coulomb coupling and relative orientation of transition dipole moments for a J-aggregate ( $\theta < 54.7^\circ$ ) and H-aggregate ( $54.7^\circ < \theta < 90^\circ$ ) using point-dipole approximation. (f) Schematic illustration of stacking patterns in push-pull polymers and form I, II polymorphs.

### 3. Conclusion

We have shown that a core-shell model is of enormous utility in analyzing P-RSoXS data to extract polymer chain orientation relative to the fibril geometry and locate variations in crystal-amorphous interphase characteristics for three different conjugated polymers: P3HT, PffBT4T-2OD, and PDPP3T. Our simulations reveal that  $q$ -dependence of anisotropy occurs *only* for systems having more than two material/density phases with numerically different optical constants. Simulation results resembling experimental data are obtained when the core is oriented and the shell is not, and the core and the shell share a density that is higher than the isotropic matrix. Different polymers exhibit different thicknesses of the crystal-amorphous interphase (shell). We also demonstrated that the direction of scattering anisotropy can be used to diagnose fibril type, with P3HT being type II and PffBT4T-2OD and PDPP3T being type I. The unique capability of P-RSoXS to derive contrast from regions having distinct orientation as well as density should find wide application across the vast number of important commodity and specialty semicrystalline polymers. In concert with other characterization methods, P-RSoXS should provide information essential to understanding and controlling path-dependent morphology evolution in soft materials, enabling accelerated process and material design for improved function.

### 4. Experimental Section

*Sample preparation:* All sample processing was done in a  $N_2$  glovebox. Blend samples were prepared following methods outlined in literature.<sup>[7e, 7g, 31]</sup> The neat film preparation protocols are given below.

PffBT4T-2OD (Solarmer)<sup>1</sup> solution was prepared in a solvent mixture of chlorobenzene (CB) and 1,2-dichlorobenzene (o-DCB) (1:1 volume ratio) with 3 % by volume fraction of DIO and concentration 9 mg.mL<sup>-1</sup>. All solvents were procured from Sigma Aldrich. The solution was stirred on a hot plate at 100 °C and left overnight. Before spin-coating, the polymer solution was preheated on a hot plate at 110 °C. Films were spin-coated from the warm polymer solution on the preheated substrate at 84 rad.s<sup>-1</sup> (800 rpm, 1 rad.s<sup>-1</sup> = 9.5 rpm).

PDPP3T (Solarmer) solution was prepared in chloroform + CB (20:80) mixed solvent with concentration 6 mg/mL and stirred on a hot plate at 70 °C and left overnight. Films were spin-coated at 1000 rpm with solution and substrate at room temperature (RT). After casting the films were annealed at 150 °C for 10 min.

P3HT (4002-EE, Rieke Metals) was dissolved in a mixed solvent (1:1 volume ratio) of cyclohexanone (CHN) (Sigma Aldrich) and CB (Sigma Aldrich) with total polymer concentration of 20 mg.mL<sup>-1</sup> and stirred overnight at 30 °C. Films were prepared by spin-casting at 2000 rpm with solution and substrate at RT. After casting the neat samples were annealed at 150 °C for 20 min, and the blend samples were annealed at 80 °C (for P3HT Blend 80C) and 150 °C (for P3HT Blend 150C) for 20 min.

Films were cast on top of a sacrificial Poly(sodium 4-styrenesulfonate) (NaPSS) (Sigma-Aldrich) layer on glass substrates. The dry films were scored with a scalpel and introduced in a bath of deionized (DI) water. The NaPSS layer was dissolved by the water leaving the semiconducting polymer film floating on surface. The floating films were then picked up on 100 nm silicon nitride windows (Norcada) for P-RSoXS measurements and TEM grids (Pelco) for LAADF-STEM measurements. GIWAXS and AFM experiments were performed on identical films cast on Si substrates.

*AFM measurements:* AFM images were recorded using a commercial atomic force microscope (Asylum MFP-3D) in tapping mode.

---

<sup>1</sup> Certain commercial equipment, instruments, materials and software are identified in this paper in order to specify the experimental procedure adequately. Such identification is not intended to imply recommendation or endorsement by NIST, nor is it intended to imply that the materials or equipment identified are necessarily the best available for the purpose.

**LAAADF-STEM measurements:** LAAADF-STEM images were acquired with a FEI Titan 80-300 at operating voltage of 300 kV. A 10 micron probe-forming aperture was employed to maximize the depth of focus resulting in a probe convergence angle of 3 mrad and a probe current of 60 pA. An annular dark field detector was employed to collect the scattered dark-field image signal over an angular range of 17 mrad to 96 mrad.

**GIWAXS measurements:** GIWAXS measurements were performed at the ALS beamline 7.3.3<sup>[32]</sup> with a beam energy of 10 keV. The 2D scattering patterns were collected at an X-ray incidence angle of 0.14° with a Pilatus 2M detector having a pixel size of 0.172 μm and placed at ≈ 300 mm from the sample. The data were analyzed using Nika<sup>[33]</sup> package in Igor Pro.

**P-RSoXS measurements:** P-RSoXS measurements were performed in transmission geometry at the ALS beamline 11.0.1.2.<sup>[34]</sup> The 2-D scattering patterns were collected using a Peltier cooled (-45 °C) in-vacuum CCD detector (PI-MTE, Princeton Instruments, 2048x2048 pixels). Data were collected at selected energies across the C K-edge (280 eV to 290 eV) with two different incident X-ray polarization (horizontal and vertical with respect to lab frame), and analyzed using a custom version of Nika package in Igor Pro.

## Supporting Information

Supporting Information is available from the Wiley Online Library or from the author.

## Acknowledgements

The authors gratefully acknowledge Jongkuk Ko (Seoul National University, Seoul), Long Ye (North Carolina State University) and Lee Richter (NIST) for providing the P3HT and PffBT4T-2OD neat and blend samples. X-ray data acquisition was supported by National Science Foundation grant DMR-1207032. X-ray data were acquired at the Advanced Light Source, which was supported by the Director, Office of Science, Office of Basic Energy Sciences, of the U.S. Department of Energy under Contract DE-AC02-05CH11231. Beamline support at beamline 11.0.1.2 was provided by A. L. D. Kilcoyne and C. Wang. Support at beamline 7.3.3 was provided by C. Zhu and E. Schaible. We thank

This article is protected by copyright. All rights reserved.

Z. Peng and S. Kashani for calculating the persistence length, Indunil Angunawela (NCSU) for providing the UV-Vis spectrum, GIWAXS and optical constants of PDPP3T, and Wei Ma (Xi'an Jiaotong University) for providing the optical constants of PffBT4T-2OD.

## References

- [1] a) S. R. Forrest, *Nature* **2004**, 428, 911; b) D. Chen, J. Yao, L. Chen, J. Yin, R. Lv, B. Huang, S. Liu, Z.-G. Zhang, C. Yang, Y. Chen, Y. Li, *Angewandte Chemie International Edition* **2018**, 57, 4580; c) Y. Sun, M. Chang, L. Meng, X. Wan, H. Gao, Y. Zhang, K. Zhao, Z. Sun, C. Li, S. Liu, H. Wang, J. Liang, Y. Chen, *Nature Electronics* **2019**, 2, 513; d) Z. Liu, X. Chen, S. Huang, H. Guo, F. Wu, J. Wang, J. Liu, X. Huang, L. Chen, Y. Chen, *Chemical Engineering Journal* **2021**, 419, 129532; e) G. Wang, L. W. Feng, W. Huang, S. Mukherjee, Y. Chen, D. Shen, B. Wang, J. Strzalka, D. Zheng, F. S. Melkonyan, J. Yan, J. F. Stoddart, S. Fabiano, D. M. DeLongchamp, M. Zhu, A. Facchetti, T. J. Marks, *Proc Natl Acad Sci U S A* **2020**, 117, 17551.
- [2] a) A. Henzen, J. van de Kamer, *Journal of the Society for Information Display* **2006**, 14, 437; b) J. Mei, Y. Diao, A. L. Appleton, L. Fang, Z. Bao, *Journal of the American Chemical Society* **2013**, 135, 6724.
- [3] a) K. Myny, S. Steudel, P. Vicca, S. Smout, M. J. Beenhakkers, N. A. J. M. van Aerle, F. Furthner, B. van der Putten, A. K. Tripathi, G. H. Gelinck, J. Genoe, W. Dehaene, P. Heremans, in *Applications of Organic and Printed Electronics: A Technology-Enabled Revolution*, DOI: 10.1007/978-1-4614-3160-2\_7 (Ed: E. Cantatore), Springer US, Boston, MA **2013**, p. 133; b) J. Xu, H.-C. Wu, C. Zhu, A. Ehrlich, L. Shaw, M. Nikolka, S. Wang, F. Molina-Lopez, X. Gu, S. Luo, D. Zhou, Y.-H. Kim, G.-J. N. Wang, K. Gu, V. R. Feig, S. Chen, Y. Kim, T. Katsumata, Y.-Q. Zheng, H. Yan, J. W. Chung, J. Lopez, B. Murmann, Z. Bao, *Nature Materials* **2019**, 18, 594.
- [4] a) E. Bihar, Y. Deng, T. Miyake, M. Saadaoui, G. G. Malliaras, M. Rolandi, *Scientific Reports* **2016**, 6, 27582; b) D. Khodagholy, V. F. Curto, K. J. Fraser, M. Gurfinkel, R. Byrne, D. Diamond, G. G. Malliaras, F. Benito-Lopez, R. M. Owens, *Journal of Materials Chemistry* **2012**, 22, 4440.

Received: ((will be filled in by the editorial staff))

Revised: ((will be filled in by the editorial staff))

Published online: ((will be filled in by the editorial staff))

- [5] a) *Nature Materials* **2013**, 12, 591; b) C. Müller, L. Ouyang, A. Lund, K. Moth-Poulsen, M. M. Hamedi, *Advanced materials (Deerfield Beach, Fla.)* **2019**, 31, e1807286; c) I. McCulloch, *Nature Materials* **2005**, 4, 583.
- [6] a) R. Steyrlleuthner, R. Di Pietro, B. A. Collins, F. Polzer, S. Himmelberger, M. Schubert, Z. Chen, S. Zhang, A. Salleo, H. Ade, A. Facchetti, D. Neher, *J Am Chem Soc* **2014**, 136, 4245; b) N. A. Ran, S. Roland, J. A. Love, V. Savikhin, C. J. Takacs, Y.-T. Fu, H. Li, V. Coropceanu, X. Liu, J.-L. Brédas, G. C. Bazan, M. F. Toney, D. Neher, T.-Q. Nguyen, *Nature Communications* **2017**, 8, 79; c) L. Yang, S. Zhang, C. He, J. Zhang, Y. Yang, J. Zhu, Y. Cui, W. Zhao, H. Zhang, Y. Zhang, Z. Wei, J. Hou, *Chemistry of Materials* **2018**, 30, 2129.
- [7] a) N. E. Persson, S. Engmann, L. J. Richter, D. M. DeLongchamp, *Chemistry of Materials* **2019**, 31, 4133; b) A. Salleo, *Materials Today* **2007**, 10, 38; c) G. Qu, J. J. Kwok, Y. Diao, *Accounts of Chemical Research* **2016**, 49, 2756; d) K. Vakhshouri, B. H. Smith, E. P. Chan, C. Wang, A. Salleo, C. Wang, A. Hexemer, E. D. Gomez, *Macromolecules* **2016**, 49, 7359; e) H. W. Ro, J. M. Downing, S. Engmann, A. A. Herzing, D. M. DeLongchamp, L. J. Richter, S. Mukherjee, H. Ade, M. Abdelsamie, L. K. Jagadamma, A. Amassian, Y. H. Liu, H. Yan, *Energy & Environmental Science* **2016**, 9, 2835; f) W. Ma, G. Yang, K. Jiang, J. H. Carpenter, Y. Wu, X. Meng, T. McAfee, J. Zhao, C. Zhu, C. Wang, H. Ade, H. Yan, *Advanced Energy Materials* **2015**, 5, 1501400; g) Y. Liu, J. Zhao, Z. Li, C. Mu, W. Ma, H. Hu, K. Jiang, H. Lin, H. Ade, H. Yan, *Nat Commun* **2014**, 5, 5293; h) N. Kleinhenz, N. Persson, Z. Xue, P. H. Chu, G. Wang, Z. Yuan, M. A. McBride, D. Choi, M. A. Grover, E. Reichmanis, *Chemistry of Materials* **2016**, 28, 3905.
- [8] S. L. Gras, L. J. Waddington, K. N. Goldie, *Methods Mol Biol* **2011**, 752, 197.
- [9] T. Ferron, M. Pope, B. A. Collins, *Phys Rev Lett* **2017**, 119.
- [10] a) B. A. Collins, J. E. Cochran, H. Yan, E. Gann, C. Hub, R. Fink, C. Wang, T. Schuettfort, C. R. McNeill, M. L. Chabinyc, H. Ade, *Nat Mater* **2012**, 11, 536; b) E. Gann, B. A. Collins, M. Tang, J. R. Tumbleston, S. Mukherjee, H. Ade, *Journal of Synchrotron Radiation* **2016**, 23, 019074.
- [11] a) J. R. Tumbleston, B. A. Collins, L. Q. Yang, A. C. Stuart, E. Gann, W. Ma, W. You, H. Ade, *Nat Photonics* **2014**, 8, 385; b) S. Mukherjee, C. M. Proctor, J. R. Tumbleston, G. C. Bazan, T. Q. Nguyen, H. Ade, *Advanced Materials* **2015**, 27, 1105; c) W. Ma, J. R. Tumbleston, M. Wang, E. Gann, F. Huang, H. Ade, *Advanced Energy Materials* **2013**, 3, 864; d) F. Liu, C. Wang, J. K. Baral, L. Zhang, J. J. Watkins, A. L. Briseno, T. P. Russell, *Journal of the American Chemical Society* **2013**, 135, 19248; e) W. Ma, L. Ye, S. Q. Zhang, J. H. Hou, H. Ade, *Journal of Materials Chemistry C* **2013**, 1, 5023.
- [12] D. Wu, M. Kaplan, H. W. Ro, S. Engmann, D. A. Fischer, D. M. DeLongchamp, L. J. Richter, E. Gann, L. Thomsen, C. R. McNeill, X. Zhang, *Chemistry of Materials* **2018**, 30, 1924.

This article is protected by copyright. All rights reserved.

- [13] a) J. H. Litofsky, E. D. Gomez, *MRS Communications* **2019**, 9, 1168; b) J. H. Litofsky, Y. Lee, M. P. Aplan, B. Kuei, A. Hexemer, C. Wang, Q. Wang, E. D. Gomez, *Macromolecules* **2019**, 52, 2803; c) Y. Diao, Y. Zhou, T. Kurosawa, L. Shaw, C. Wang, S. Park, Y. Guo, J. A. Reinspach, K. Gu, X. Gu, B. C. K. Tee, C. Pang, H. Yan, D. Zhao, M. F. Toney, S. C. B. Mannsfeld, Z. Bao, *Nature Communications* **2015**, 6, 7955.
- [14] a) A. Keller, *Physikalische Blätter* **1983**, 39, 178; b) L. C. Sawyer, R. T. Chen, M. G. Jamieson, I. H. Musselman, P. E. Russell, *Journal of Materials Science* **1993**, 28, 225; c) J. Adamcik, R. Mezzenga, *Macromolecules* **2012**, 45, 1137; d) T. Yamamoto, *The Journal of Chemical Physics* **2013**, 139, 054903; e) J. M. G. Cowie, *Polymers: Chemistry and Physics of Modern Materials, 2nd Edition*, Taylor & Francis, **1991**; f) P. J. Phillips, *Rep Prog Phys* **1990**, 53, 549.
- [15] I. Monnaie, *Phd Thesis 1 (Research TU/e / Graduation TU/e)*, Technische Universiteit Eindhoven, Eindhoven, **2015**.
- [16] a) A. Herland, P. Björk, P. R. Hania, I. G. Scheblykin, O. Inganäs, *Small* **2007**, 3, 318; b) A. Barkaoui, B. Tlili, A. Vercher-Martínez, R. Hamblin, *Computer Methods and Programs in Biomedicine* **2016**, 134, 69.
- [17] a) E. F. Eikenberry, B. Childs, S. B. Sheren, D. A. D. Parry, A. S. Craig, B. Brodsky, *Journal of Molecular Biology* **1984**, 176, 261; b) B. Brodsky, E. F. Eikenberry, in *Methods in Enzymology*, Vol. 82, Academic Press **1982**, p. 127.
- [18] a) J. Saska, G. Gonel, Z. I. Bedolla-Valdez, S. D. Aronow, N. E. Shevchenko, A. S. Dudnik, A. J. Moulé, M. Mascal, *Chemistry of Materials* **2019**, 31, 1500; b) N. D. Treat, M. A. Brady, G. Smith, M. F. Toney, E. J. Kramer, C. J. Hawker, M. L. Chabinyc, *Advanced Energy Materials* **2011**, 1, 82.
- [19] a) H. Yang, T. J. Shin, L. Yang, K. Cho, C. Y. Ryu, Z. Bao, *Advanced Functional Materials* **2005**, 15, 671; b) H. Li, J. Mei, A. L. Ayzner, M. F. Toney, J. B. H. Tok, Z. Bao, *Organic Electronics* **2012**, 13, 2450; c) M. Li, D. K. Mangalore, J. Zhao, J. H. Carpenter, H. Yan, H. Ade, H. Yan, K. Müllen, P. W. M. Blom, W. Pisula, D. M. de Leeuw, K. Asadi, *Nature Communications* **2018**, 9, 451.
- [20] D. S. Germack, C. K. Chan, B. H. Hamadani, L. J. Richter, D. A. Fischer, D. J. Gundlach, D. M. DeLongchamp, *Appl Phys Lett* **2009**, 94, 233303.
- [21] B. Watts, S. Swaraj, D. Nordlund, J. Luning, H. Ade, *J Chem Phys* **2011**, 134, 024702.
- [22] I. Livsey, *Journal of the Chemical Society, Faraday Transactions 2: Molecular and Chemical Physics* **1987**, 83, 1445.

This article is protected by copyright. All rights reserved.

- [23] M. Brinkmann, P. Rannou, *Advanced Functional Materials* **2007**, 17, 101.
- [24] J. Martín, N. Stingelin, D. Cangialosi, *The Journal of Physical Chemistry Letters* **2018**, 9, 990.
- [25] I. Angunawela, M. M. Nahid, M. Ghasemi, A. Amassian, H. Ade, A. Gadisa, *ACS Applied Materials & Interfaces* **2020**, 12, 26239.
- [26] W. Zhang, E. D. Gomez, S. T. Milner, *Macromolecules* **2014**, 47, 6453.
- [27] a) J. Rivnay, M. F. Toney, Y. Zheng, I. V. Kauvar, Z. Chen, V. Wagner, A. Facchetti, A. Salleo, *Advanced Materials* **2010**, 22, 4359; b) G. Pirotte, P. Verstappen, D. Vanderzande, W. Maes, *Advanced Electronic Materials* **2018**, 4, 1700481; c) M. Brinkmann, E. Gonthier, S. Bogen, K. Tremel, S. Ludwigs, M. Hufnagel, M. Sommer, *ACS Nano* **2012**, 6, 10319; d) P. M. Beaujuge, J. M. Fréchet, *Journal of the American Chemical Society* **2011**, 133, 20009; e) X. Zhang, L. J. Richter, D. M. DeLongchamp, R. J. Kline, M. R. Hammond, I. McCulloch, M. Heeney, R. S. Ashraf, J. N. Smith, T. D. Anthopoulos, B. Schroeder, Y. H. Geerts, D. A. Fischer, M. F. Toney, *Journal of the American Chemical Society* **2011**, 133, 15073.
- [28] a) J. Clark, J.-F. Chang, F. C. Spano, R. H. Friend, C. Silva, *Appl Phys Lett* **2009**, 94, 163306; b) F. C. Spano, C. Silva, *Annual Review of Physical Chemistry* **2014**, 65, 477.
- [29] N. J. Hestand, F. C. Spano, *Chem. Rev.* **2018**, 118, 7069.
- [30] a) N. J. Hestand, F. C. Spano, *Accounts of Chemical Research* **2017**, 50, 341; b) H. Yamagata, C. M. Pochas, F. C. Spano, *The Journal of Physical Chemistry B* **2012**, 116, 14494.
- [31] a) J. Ko, J. Song, W. T. Choi, T.-H. Kim, Y.-S. Han, J. Lim, C. Lee, K. Char, *Macromolecular Research* **2018**, 26, 623; b) L. Ye, S. Zhang, W. Ma, B. Fan, X. Guo, Y. Huang, H. Ade, J. Hou, *Advanced Materials* **2012**, 24, 6335.
- [32] A. Hexemer, W. Bras, J. Glossinger, E. Schaible, E. Gann, R. Kirian, A. MacDowell, M. Church, B. Rude, H. Padmore, *J. Phys.: Conf. Ser.* **2010**, 247, 012007.
- [33] J. Ilavsky, *J Appl Crystallogr* **2012**, 45, 324.
- [34] E. Gann, A. T. Young, B. A. Collins, H. Yan, J. Nasiatka, H. A. Padmore, H. Ade, A. Hexemer, C. Wang, *Rev Sci Instrum* **2012**, 83, 045110.

This article is protected by copyright. All rights reserved.

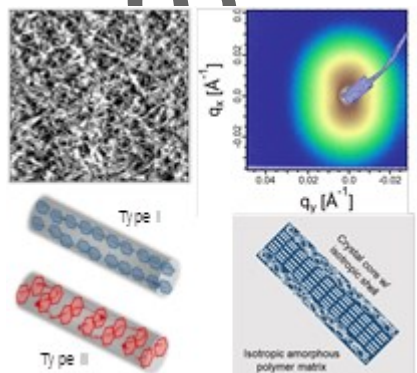
Table of contents entry:

Coupling experiments with simulations this study shows that the sign and the analysis of  $q$ -dependence of the scattering anisotropy can reveal the fibril type, internal structure of the fibrils, number of phases, densities of the different phases, as well as relative locations in the system. Results suggest that polymer homo-material films can have more than two phases.

*Subhrangsu Mukherjee\*, Eliot Gann, Masrur Morshed Nahid, Terry McAfee, Andrew A. Herzing, Dean M. DeLongchamp\*, Harald Ade\**

### Orientational ordering within semiconducting polymer fibrils

ToC figure



This article is protected by copyright. All rights reserved.